Energy Engineering

Tech Science Press

https://doi.org/10.32604/ee.2026.075066

ARTICLE

A Double-Time-Scale Dynamic Reactive Power Optimization Method for the AC/DC Hybrid Power Grid Incorporating UPFC

Wei Yin[1,*], Jun Wang[1], Ming Tong[1], Zhijun Chen[1], Ke Zhang[1], Meiqing Huang[2], Ran Gu[2] and Keman Lin[2]

[1]State Grid Suzhou Power Supply Company, Suzhou, China
[2]College of Electrical and Power Engineering, Hohai University, Nanjing, China

*Corresponding Author: Wei Yin. Email: moiww@sohu.com

Received: 24 October 2025; Accepted: 29 January 2026; Published: 18 June 2026

ABSTRACT: With the high penetration of renewable energy and the rapid development of AC/DC (Alternating Current/Direct Current) hybrid power grid, the power grid is confronted with challenges such as frequent voltage fluctuations and insufficient dynamic reactive power reserves. Full utilization of unified power flow controller (UPFC) in dynamic voltage regulation is of great significance for mitigating voltage excursions of the power grid. This paper proposes a double-time-scale dynamic reactive power optimization method for the AC/DC hybrid power grid with UPFC. A control framework for reactive power optimization of slow-time-scale and fast-time-scale is constructed incorporating the LCC-HVDC and UPFC. In this method, the slow-time-scale aims to improve the voltage profiles and reduce the system cost by setting the voltage regulation weight coefficients based on trajectory sensitivity to preserve reactive power regulation capability. The fast-time-scale adopts an adaptive feedback control mechanism. When slow-time-scale optimization is insufficient to keep the voltage within a safe range, it adjusts the real-time reactive power output of the UPFC, and damps rapid voltage swings accordingly. By implementing the additional fast-time-scale control method, the frequent variations of both the Photovoltaic (PV) and load are managed for the reactive power compensation. Case studies on a modified IEEE-30 bus system demonstrate that compared with the conventional control method, the proposed method reduces the maximum voltage deviation by 3.17% compared to the baseline, while ensuring the economic efficiency.

KEYWORDS: AC/DC hybrid power grid; UPFC; double-time-scale; dynamic reactive power optimization; trajectory sensitivity

1 Introduction

In recent years, photovoltaic and wind generation have experienced unprecedented growth. The fluctuation and uncertainty of renewable energy output lead to frequent voltage exceeding the limit in the power system [1–3], urgently requiring reasonable and efficient reactive power and voltage management strategies to ensure the safe and reliable operation of the power system. As DC transmission plays an increasingly important role in the operation of power grid [4,5], AC/DC hybrid power grid has become a new stage in the development and evolution of power grid. It has unique structural and operational characteristics but also faces severe safety challenges [6–8].

Commonly used discrete reactive power compensation resources include on-load tap changer (OLTC) and capacitor bank (CB) [9]. These devices have features such as large capacity, low cost, and excellent steady-state regulation performance [10], but are difficult to handle the need of rapid reactive power compensation. The continuous reactive power compensation resources include static var compensator (SVC) and UPFC [11]. These devices have features such as high reliability, low loss, and fast dynamic response, but the cost of reactive power compensation is relatively high [12]. The current studies focus on coordinating the discrete and continuous resources for the reactive power compensation to achieve the desired performance at a relative low cost.

The coordinated reactive power compensation methods are primarily categorized into centralized optimization and distributed optimization. Reference [13] proposed a centralized control method based on adaptive virtual impedance, which achieves accurate reactive power sharing by compensating for voltage drop across the feeders. Reference [14] proposed the centralized method based on adaptive Q-V droop coefficients, implementing the control method from [13]. Reference [15] proposed a simplified distributed control strategy for reactive power sharing and voltage/frequency restoration, which reduces the computational burden of local controllers. Recently, advanced signal-decomposition-based coordinated Volt/Var control schemes for PV-rich distribution networks have also been reported in [16]. References [17,18] established a double-time-scale reactive power and voltage optimization model for distribution networks, achieving coordinated control of voltage regulating devices with different time response characteristics. References [19–21] established a multi-time-scale reactive power optimization model for distribution networks, coordinating and cooperating with various types of control device to enhance system voltage stability and power quality.

Reference [22] established a mathematical model of the distribution network containing photovoltaic power generation systems, electric vehicles, energy storage systems and reactive power compensation device SVG for reactive power optimization research, and used the particle swarm optimization (PSO) algorithm for solution. Reference [23] proposed a second-order cone relaxation model for reactive power optimization in three-phase unbalanced active distribution networks, transforming the optimization problem into a mathematical programming form with a convex feasible region for solution. Reference [24] proposed a novel data-driven reactive power optimization strategy for distribution networks based on autoencoder-constrained temporal convolutional networks, which coordinates various reactive power regulation devices such as photovoltaic inverters and capacitor banks at multiple time scales through three stages. Reference [25] proposed a multi-objective function reactive power optimization method oriented towards system weak link analysis, and used an improved adaptive genetic algorithm for solution. Reference [26] established a multi-objective reactive power and voltage control optimization model that considers both network loss and voltage deviation, and proposed a whale swarm model solution algorithm based on the combination of the traditional whale algorithm and particle swarm optimization. However, the coordination between different time scales for reactive power compensation in transmission network remains insufficiently addressed.

UPFC is a power electronic controller consisting of two back-to-back voltage-source converters (series and shunt) that regulates both active and reactive power flow in transmission lines [27]. UPFC achieves continuous reactive power regulation through the decoupling control of active and reactive power. Studying the dynamic reactive power optimization problem taking UPFC into account is conducive to further improving the safety and economy of power grid operation while fully utilizing the regulation capability of UPFC [28]. Reference [29] established a multi-terminal injection power model and power equation for UPFC, considering its coordinated optimization with discrete reactive power devices. Based on the idea of reducing the constraint of the number of reactive power device actions to the regulation cost, a two-stage reactive power optimization algorithm containing only continuous variables is proposed. Reference [30] used a new sensitivity analysis index to determine the optimal size and position of UPFC. The simulation results

show that it significantly improves network loss and total harmonic distortion. Reference [31] established a multi-objective reactive power optimization model taking UPFC into account, proposed a multi-stage multi-objective reactive power optimization algorithm, and finally conducted a case study test based on the actual equivalent system of Nanjing West Ring Network to verify the effectiveness of the multi-stage algorithm and the application prospects of UPFC in the field of reactive power optimization. Achieving coordinated optimization between UPFC and other devices to meet the system's flexible regulation requirements at different time scales remains a major research focus.

In recent years, with the increasing penetration of DC loads and new energy sources, the voltage regulation of AC/DC hybrid power grids has gradually evolved from the static reactive power optimization of traditional transmission grids to a comprehensive optimization problem involving multi-device collaboration, multiple objectives, multiple time scales, and uncertainties. Reference [32] incorporated inverters, voltage control devices and distribution and consumption side strategies into a unified AC/DC hybrid network optimization, and characterizes the operational risks introduced by prediction errors through risk constraints, thereby forming a more engineering day-ahead scheduling. Reference [33] considers the strong dependence of commutative DC systems such as LCC-HVDC on dynamic reactive power support during fault processes. Researchers propose a method for order reduction equivalence and dynamic reactive power reserve evaluation for dynamic processes at the hundred-millisecond level, providing computable indicators for dynamic reactive power optimization and safety margin constraints. A multi-source dynamic reactive power cooperative optimization control strategy for DC lockout/commutation failure transient overvoltage has been developed to enhance voltage stability in complex fault scenarios [34]. In addition, reactive power optimization in AC/DC hybrid power grids often needs to simultaneously confront issues such as uncertainty and the coupling of multi-agent decision-making. Therefore, risk avoidance and game theory methods in the field of power system optimization are also frequently employed to provide modeling [35,36].

There are still several limitations in existing domestic and international studies. First, most double- or multi-time-scale Volt/Var optimization strategies are developed for radial distribution networks or pure AC systems, and the interaction between AC and DC subsystems in hybrid networks is seldom explicitly modelled; the influence of the reactive power demand of LCC-HVDC links on time-coupled voltage control is often described in a simplified or quasi-static way [37]. Second, the coordination among heterogeneous devices across different time scales remains insufficient: discrete equipment such as OLTCs and CBs is usually scheduled only on slow horizons, while fast FACTS (Flexible AC transmission system) devices are either neglected or operated under fixed local control, without explicitly preserving dynamic reactive power reserve for subsequent regulation [38]. Finally, existing works rarely exploit the trajectory-sensitivity information of AC/DC hybrid power grids to design adaptive weighting mechanisms for different devices, which is essential to avoid over-utilization of fast resources and to guarantee coordinated operation over the whole optimization process [39]. These research gaps motivate the double-time-scale dynamic reactive power optimization method based on the trajectory-sensitivity-based adaptive weighting mechanism for AC/DC hybrid power grids with UPFC proposed in this paper.

Based on the above research foundation, this paper proposes the a double-time-scale dynamic reactive power optimization method of the AC/DC hybrid power grid with UPFC. In this method, the slow-time scale aims to improve the voltage profiles and reduce the system cost by setting the voltage regulation weight coefficients based on trajectory sensitivity to preserve reactive power regulation capability. The fast-time-scale adopts an adaptive feedback control mechanism to adjust the real-time reactive power output of the UPFC, and reduces the voltage fluctuation accordingly. The adaptive feedback control procedure is activated to optimize and adjust slow-time-scale operation scheme when the real-time voltage magnitude exceeds the preset threshold. The effectiveness of the proposed method is verified by simulation.

The major contributions of this paper are summarized as follows:

(1) The double-time-scale reactive power optimization method is applied to coordinate fast time-scale devices and slow time-scale devices in the AC/DC hybrid grids incorporating UPFC. The proposed method coordinates slow-time-scale (1 h) and fast-time-scale (5 min) optimizations hierarchically. This structure coordinates different devices with discrete devices (OLTCs, CBs) for slow-time-scale regulation, and continuous devices (UPFC) for fast-time-scale regulation. This framework effectively balances the operational cost against the need for the rapid response due to the fluctuations from the renewables and loads.

(2) A trajectory-sensitivity-based adaptive weighting mechanism is proposed to regulate the regulation costs. The proposed mechanism dynamically assigns voltage regulation cost weights to OLTCs, CBs, and the UPFC according to their real-time trajectory sensitivities. In this way, the slow-time-scale optimization preferentially utilizes discrete devices and deliberately pre-serves the UPFC's regulation margin for the subsequent fast-time-scale layer. This mechanism ensures that the slow-time-scale optimization prioritizes the discrete devices while conserving the capacity of the UPFC for the subsequent fast-time-scale regulation, thereby enhancing the overall coordination and robustness of the double-time-scale control method.

The remainder of this paper is organized as follows: Section 2 introduces the modeling of the AC/DC hybrid power grid with LCC-HVDC and UPFC. Section 3 introduces the formulation of the proposed double-time-scale dynamic reactive power optimization method. Section 4 presents the case study. Finally, Section 5 concludes the paper.

2 Dynamic Model of AC/DC Hybrid Power Grid

AC/DC hybrid power grids have both AC and DC components, which makes reactive power optimization and voltage regulation more complex than in AC power grids. The grid includes renewables and reactive power compensation devices that adjust the node voltage in AC/DC hybrid power grid. Commonly used continuous devices-FACTS devices such as UPFC and SVC, discrete devices such as OLTC and CB to coordinate these devices to achieve a reasonable reactive power distribution. The randomness and fluctuation of the output of renewable energy sources increase the risk of voltage violation. Meanwhile, the operation of line commutated converter based high voltage direct current (LCC-HVDC) imposes strict demand on reactive power support near landing point. Therefore, this section constructs dynamic models of key devices in AC/DC hybrid power grid including photovoltaic, LCC-HVDC, UPFC, OLTC, and CB. Firstly, a temporal probability model of the photovoltaic power generation system is introduced to represent the uncertainty of its output. Next, the LCC-HVDC model is built to describe the power exchange relationship between the AC and DC network considering the power transmission demand of the DC terminal. Finally, the models of reactive power compensation devices are established, and their dynamic characteristics of reactive power regulation are analyzed. This paper uses UPFC as a continuous device, along with OLTC and CB as discrete devices. The establishment of these models provide the necessary theoretical basis and mathematical description for the collaborative optimization of different complementary resources in Section 2.

2.1 PV Model

The power generation characteristics of photovoltaic systems are closely related to solar irradiation conditions. Due to the combined influence of geographical and environmental conditions, the intensity of solar irradiation shows significant differences. The Beta model is used to represent the distribution of solar irradiation within a day [40]. Then, the temporal probability distribution model of photovoltaic power generation is:

$$F\left(P_{\mathrm{PV},t}\right)=\frac{\Gamma\left(\alpha+\beta\right)}{\Gamma\left(\alpha\right)\Gamma\left(\beta\right)}\left(\frac{P_{\mathrm{PV},t}}{P_{\mathrm{PV,max}}}\right)^{\alpha-1}\left(1-\frac{P_{\mathrm{PV},t}}{P_{\mathrm{PV,max}}}\right)^{\beta-1} \tag{1}$$

$$P_{\mathrm{PV},t}=rA\eta \tag{2}$$

$$\Gamma\left(x\right)=\int_0^{\infty}t^{x-1}\mathrm{e}^{-t}\mathrm{dt} \tag{3}$$

where, $F\left(P_{\mathrm{PV},t}\right)$ is the probability value of the active power generated by PV. $P_{\mathrm{PV,max}}$ is the maximum output by PV. $P_{\mathrm{PV},t}$ is the actual output by PV at time t. $\Gamma\left(\cdot\right)$ is the Gamma function. α and β are two adjustable parameters of the Beta model, respectively [41]. r is the solar irradiance. A is the total area of photovoltaic panels. η is the photoelectric conversion efficiency. x is the input parameter of the Gamma function. t is an integral variable.

2.2 LCC-HVDC Model

LCC-HVDC is the key component of the AC/DC hybrid power grid which connects the AC and DC sub-systems. To analyze the characteristics of AC/DC hybrid power grid, it is necessary to analyze the active and reactive power interactions between the converter station and the AC system in LCC-HVDC. The mathematical model for LCC-HVDC is shown in Fig. 1 [42]. The active and reactive power absorbed by the converter station from the AC system can be calculated by Eq. (4).

$$\begin{cases}P_{si}=\dfrac{U_{si}U_{ci}\sin\left(\theta_{si}-\theta_{ci}\right)}{X_i}\\ Q_{si}=\dfrac{U_{si}\left[U_{si}-U_{ci}\cos\left(\theta_{si}-\theta_{ci}\right)\right]}{X_i}\end{cases} \tag{4}$$

where, P_{si} and Q_{si} are the active and reactive power absorbed by the converter station from the AC system, respectively. U_{si} and θ_{si} are the voltage magnitude and phase angle of the AC system, respectively. U_{ci} and θ_{ci} are the voltage magnitude and phase angle of the converter station. X_i is the equivalent reactance.

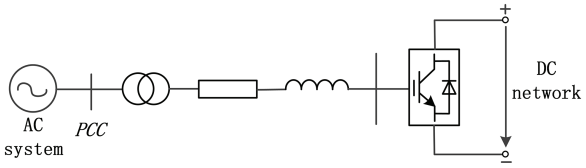

Figure 1: The structure of the LCC-HVDC.

The phase angle difference between the AC and DC buses is defined as $\delta_i=\theta_{si}-\theta_{ci}$. The impedance angle is defined as $\alpha_i=arctg\left(X_i/R_i\right)$. Then,

$$\begin{cases}P_{si}=-\left|Y_i\right|U_{si}U_{ci}\cos\left(\delta_i+\alpha_i\right)+\left|Y_i\right|U_{si}^2\cos\alpha_i\\ Q_{si}=-\left|Y_i\right|U_{si}U_{ci}\sin\left(\delta_i+\alpha_i\right)+\left|Y_i\right|U_{si}^2\sin\alpha_i\\ P_{ci}=\left|Y_i\right|U_{si}U_{ci}\cos\left(\delta_i-\alpha_i\right)-\left|Y_i\right|U_{ci}^2\cos\alpha_i\\ Q_{ci}=-\left|Y_i\right|U_{si}U_{ci}\sin\left(\delta_i-\alpha_i\right)-\left|Y_i\right|U_{ci}^2\sin\alpha_i\end{cases} \tag{5}$$

where, P_{ci} and Q_{ci} are the active and reactive power entering the converter bridge arm, respectively. Y_i is the equivalent admittance, $\left|Y_i\right|=1/\sqrt{R_i^2+X_i^2}$.

The active power transmitted by the DC system P_{di} can be expressed as,

$$P_{di} = U_{di}I_{di} = \mid Y_i \mid U_{si}U_{ci}\cos\left(\delta_i - \alpha_i\right) - \mid Y_i \mid U_{ci}^2\cos\alpha_i = P_{ci} \tag{6}$$

where, U_{di} and I_{di} are the DC voltage and current, respectively.

2.3 UPFC Model

The UPFC device consists of a shunt converter, a series converter, a DC link capacitor, a shunt transformer, a series transformer [43]. It is modeled as a series converter injecting a controllable voltage source in series with the transmission line and a shunt converter injecting a controllable current at the sending bus. The shunt converter provides shunt compensation by generating or absorbing reactive power to regulate the bus voltage and maintain the power balance, thereby supporting the series voltage injection. The configuration of UPFC is shown in Fig. 2. The voltage equation of the UPFC is portrayed in Eq. (7).

$$V_1 = -V_{12} + \mathrm{j}Z_{\mathrm{R}}I + V_{\mathrm{R}} \tag{7}$$

where, V_1 is the bus voltage of the UPFC input terminal. V_{12} is the injection voltage of the UPFC to the power grid, and the inflow is positive and the outflow is negative. Z_{R} and V_{R} are the impedance and voltage at the receiving terminal, respectively. I is the line current.

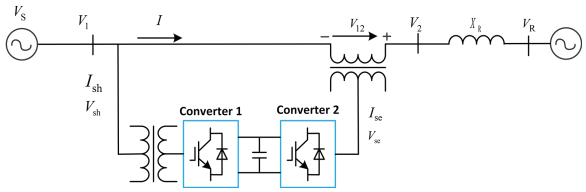

Figure 2: The structure of the UPFC.

The complex power exchanged between the AC network and the shunt converter is:

$$S_{sh} = P_{sh} + jQ_{sh} = V_1I_{sh}^* \tag{8}$$

where I_{sh} is the current between the AC network and the shunt converter.

Under steady-state conditions, when only reactive power is exchanged, it is generally assumed that V_1 and V_{sh} are in phase. Therefore, their magnitudes can be directly used in the calculations. The current flowing through the reactor is given by:

$$I_{sh} = \frac{V_1 - V_{sh}}{j\omega L_{sh}} = j\frac{V_{sh} - V_1}{\omega L_{sh}} \tag{9}$$

where V_{sh} and L_{sh} are the voltage and inductance of the shunt converter, respectively. ω is the angular frequency.

In the power grid, voltage fluctuations are mainly caused by reactive power fluctuations. The UPFC utilizes the reactive power control function of its own shunt converter to provide voltage support for the AC/DC hybrid power grid. Substituting Eqs. (10) and (11) gives the result:

$$|Q_{\max}| = \frac{\left(V_1 - V_{\mathrm{sh}}\right)V_1}{\omega L_{\mathrm{sh}}} \tag{10}$$

$$V_{sh} = \sqrt{3}V_{ph,rms} = \sqrt{3} \cdot \frac{MV_{dc}}{2\sqrt{2}} = M \cdot \sqrt{\frac{3}{8}} \cdot V_{dc} \tag{11}$$

Substituting Eq. (12) gives

$$|Q_{\max}| = \frac{V_1 \left| V_1 - M \cdot \sqrt{\frac{3}{2}} \frac{V_{\mathrm{dc}}}{2} \right|}{\omega L_{\mathrm{sh}}} \tag{12}$$

where M is the modulation index of the converter. V_{dc} is the voltage of DC link capacitor. $V_{ph,rms}$ is the effective value of the fundamental phase voltage output by the converter. The adjustable reactive power range of UPFC varies between the minimum value $Q_{\max -}$ and the maximum value $Q_{\max +}$ (the absolute values of $Q_{\max -}$ and $Q_{\max +}$ are equal to $|Q_{\max}|$).

The active and reactive power generated by UPFC are portrayed in Eqs. (13) and (14).

$$P_{12} = V_{12} \cdot I \tag{13}$$

$$Q_{12} = V_{12} \times I \tag{14}$$

where, P_{12} and Q_{12} are the active and reactive power injected into the power grid by the UPFC, respectively.

2.4 OLTC Model

The OLTC is basically a transformer. For the convenience of calculation, a virtual node j is introduced. The virtual node partitions the transformer into the ideal transformer and the equivalent impedance [44]. The model is shown in Fig. 3. The voltage ratio of OLTC is defined as 1: N, the voltages at nodes i and j are defined as U_i and U_j, respectively. Then,

$$U_j = NU_i \tag{15}$$

$$N = (1 + \Delta V_{\mathrm{OLTC}} n_{\mathrm{OLTC}}) \tag{16}$$

$$U_j = (1 + \Delta V_{\mathrm{OLTC}} n_{\mathrm{OLTC}})\, U_i \tag{17}$$

where, ΔV_{OLTC} is the voltage ratio corresponding to a single gear of OLTC. n_{OLTC} is the tap position of OLTC.

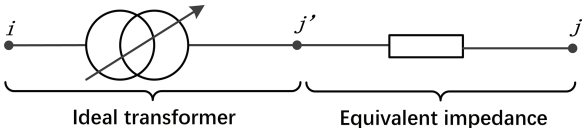

Figure 3: Equivalent model of OLTC.

This section establishes the dynamic models for the key components in the AC/DC hybrid power grid, including the photovoltaic systems, the LCC-HVDC, the UPFC, the OLTC, and the CB [45]. The photovoltaic model captures the uncertainty of the solar energy, while the LCC-HVDC addresses the power demands of the DC terminal. The UPFC, OLTC, and CB are modeled to characterize their respective voltage regulation capabilities as continuous and discrete reactive power compensation devices. These models establish the theoretical foundation for the double-time-scale optimization framework presented in Section 2.

3 The Double-Time-Scale Dynamic Reactive Power Optimization Method

3.1 The Framework of the Proposed Method

In order to coordinate the continuous and discrete resources to achieve the optimal reactive power configuration, this paper proposes a double-time-scale dynamic reactive power optimization method for AC/DC hybrid power grid with UPFC participation in regulation. The overall framework of this method is shown in Fig. 4. Each area has an individual local controller to collect data and calculate the following variables including: ① operational information of OLTC, CB and UPFC. ② predicted active and reactive power outputs of UPFC. The PSO algorithm is adopted to solve the optimization problem.

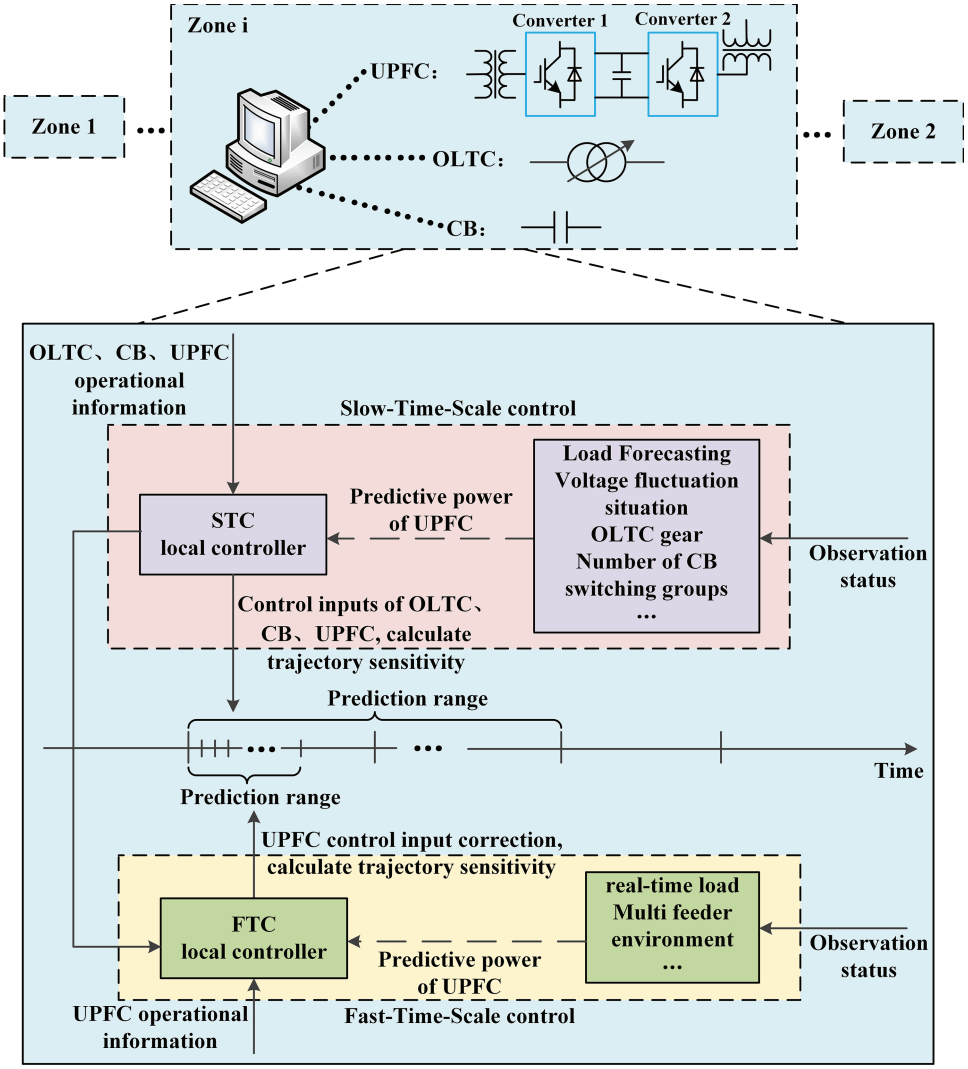

Figure 4: The framework of the proposed method.

The control scheme is optimized hourly on slow-time-scale. The control variables of OLTC, CB and UPFC are optimized based on the trajectory sensitivity method. By coordinating reactive power devices with different dynamic characteristics, this method minimizes the overall costs and preserves adequate dynamic reactive power reserve.

The reactive power output of UPFC is optimized every 5 min on fast-time-scale on the basis of the results from slow-time-scale. The fast-time-scale optimization further improves the voltage profile by adjusting the reactive power output of continuous compensation devices including UPFC. The voltage deviation of each node is calculated based on the slow-time-scale optimization results of the discrete and continuous resources. The slow-time-scale control is re-engaged to adjust the reactive power compensation when the node voltage exceeds the operation limits. Based on the current actual load and renewable energy output value, the reactive power output of UPFC is calculated to reduce the voltage deviation and improve the power quality.

3.2 The Slow-Time-Scale Optimization

3.2.1 Objective Function

The slow-time-scale aims to minimize the overall system cost, including the cost of network loss, the operation costs of OLTC and CB, and the reactive power cost of UPFC.

$$\min F_{\mathrm{STC}}(u) = \sum_{t=1}^{T} \left[\sum_{i\in\Omega_{\mathrm{b}}} \sum_{j\in N_{\mathrm{c}}(i)} \pi_t P_{\mathrm{LOSS},i}^{j}(t) + \sum_{i\in\Omega_{\mathrm{b}}^{\mathrm{OLTC}}} \sum_{j\in N_{\mathrm{c}}^{\mathrm{OLTC}}(i)} W_{\mathrm{OLTC}} C_{\mathrm{OLTC},i}^{j}(t) + \sum_{i\in\Omega_{\mathrm{b}}^{\mathrm{CB}}} W_{\mathrm{CB}} C_{\mathrm{CB},i}(t) + \sum_{i\in\Omega_{\mathrm{b}}^{\mathrm{UPFC}}} \sum_{j\in N_{\mathrm{c}}^{\mathrm{UPFC}}(i)} W_{\mathrm{UPFC}} C_{\mathrm{UPFC},i}^{j}(t) \right] \tag{18}$$

where, t is the time number, T is the optimization cycle, Ω_{b} is the node set. i and j are the number of the node, respectively. $\Omega_{\mathrm{b}}^{\mathrm{OLTC}}$, $\Omega_{\mathrm{b}}^{\mathrm{CB}}$ and $\Omega_{\mathrm{b}}^{\mathrm{UPFC}}$ are the node set connected to OLTC, CB and UPFC, respectively. $N_{\mathrm{c}}(i)$ is the child node set of node i. $N_{\mathrm{c}}^{\mathrm{OLTC}}(i)$ and $N_{\mathrm{c}}^{\mathrm{UPFC}}(i)$ is the child node set of node i connected to OLTC and UPFC, respectively. π_t is the unit cost of network loss. $P_{\mathrm{LOSS},i}^{j}(t)$ is the network loss. W_{OLTC}, W_{CB} and W_{UPFC} are the voltage regulation cost weight coefficients of OLTC, CB and UPFC, respectively. $C_{\mathrm{OLTC},i}^{j}(t)$, $C_{\mathrm{CB},i}(t)$ and $C_{\mathrm{UPFC},i}^{j}(t)$ are the reactive power regulation cost of OLTC, CB and UPFC, respectively.

In order to investigate the dynamic response characteristics of various voltage regulation devices to the power grid state, the trajectory sensitivity of AC/DC hybrid power grid is defined. The trajectory sensitivity of AC/DC hybrid power grid exhibits time-varying characteristics, reflecting the influence of parametric changes on the system operational states. The specific steps are as follows.

(1) Describe the variation of variables with control quantities using trajectory mapping

In this paper, $\Phi_x(u,t)$ and $\Phi_y(u,t)$ are defined to represent the change trajectories of state variables and algebraic variables in the AC/DC hybrid power grid, respectively [46]. Then,

$$\begin{cases} x(t) = \Phi_x(u,t) \\ y(t) = \Phi_y(u,t) \end{cases} \tag{19}$$

where, $x(t)$ and $y(t)$ are the state variables and algebraic variables of the AC/DC hybrid power grid at time t, respectively. u is the control variable, $u = \begin{bmatrix} n_{\mathrm{OLTC}} & n_{\mathrm{CB}} & Q_{\mathrm{UPFC}} \end{bmatrix}$.

(2) Perform first-order linearization at the running point

The variables $x(t)$ and $y(t)$ are expanded by the Taylor series at $u = u_0$, with the higher-order terms of the control variable change Δu being neglected [47]. The changes in state and algebraic variables caused by control variable change at time t are approximately expressed as:

$$\begin{cases} x(t) = \Phi_x(u,t) \\ y(t) = \Phi_y(u,t) \end{cases} \tag{20}$$

$$\begin{cases} \Delta x(t) = \dfrac{\partial \Phi_x(u_0, t)}{\partial u_0}(u - u_0) = x_u(t)\,\Delta u \\ \Delta y(t) = \dfrac{\partial \Phi_y(u_0, t)}{\partial u_0}(u - u_0) = y_u(t)\,\Delta u \end{cases} \tag{21}$$

where, $x_u(t)$ and $y_u(t)$ are the trajectory sensitivities of $x(t)$ and $y(t)$ with respect to u, respectively.

(3) Calculate the trajectory sensitivity by using the finite difference approximation

When Δu is sufficiently small, the trajectory sensitivities of the AC/DC hybrid power grid are as follows:

$$\begin{cases} x_u(t) \approx \lim\limits_{\Delta u \to 0} \frac{\Delta x(t)}{\Delta u} = \dfrac{\Phi_x(u_0 + \Delta u, t) - \Phi_x(u_0, t)}{\Delta u} \\ y_u(t) \approx \lim\limits_{\Delta u \to 0} \dfrac{\Delta y(t)}{\Delta u} = \frac{\Phi_y(u_0 + \Delta u, t) - \Phi_y(u_0, t)}{\Delta u} \end{cases} \tag{22}$$

(4) Calculate the sensitivity of voltage to the control quantity

The trajectory sensitivities of the control variables for OLTC, CB, and UPFC devices are calculated. The grid state variables are represented by node voltage. Then,

$$\left.\frac{\partial V}{\partial u}\right|_{u=u_k} = \frac{V(u_k + \Delta u_k) - V(u_k)}{\Delta u_k} \tag{23}$$

(5) Normalization yields the dimensionless trajectory sensitivity index

In order to avoid dimensional differences, the above equation is normalized as follows:

$$S_u = \left.\frac{\partial V}{\partial u}\right|_{u=u_k} \cdot \frac{u_{\text{base}}}{V_{\text{base}}} \tag{24}$$

where, u_{base} is the basic value of the control variable (the maximum tap position of OLTC, the maximum tap position of CB, and the reactive power basic value of UPFC). V_{base} is the voltage basic value.

During slow-time-scale voltage control, excessive use of the dynamic reactive power resources should be avoided to prevent compromising subsequent fast-time-scale voltage control. As shown in Eq. (25), the voltage regulation cost weight coefficients of different voltage regulation devices are set to be proportional to their trajectory sensitivities, ensuring the slow-time-scale voltage control scheme preserves sufficient dynamic reactive power reserve. The weight coefficients are set to $W_{\text{UPFC}} \geq W_{\text{OLTC}} \geq W_{\text{CB}}$, which also conforms to the principle "Discrete devices take priority in operation, while continuous devices perform fine adjustments". Before each slow-time-scale voltage control, the trajectory sensitivities need to be updated based on the current power grid operating status, then updating the weight coefficients.

$$C_i = kS_{u,i} \tag{25}$$

where k is the proportional parameter.

The calculation equation for the network loss in AC/DC hybrid power grid is as follows:

$$P_{\text{LOSS}}{}_{,i}^{j}(t) = \sum_{i \in \Omega_b} \sum_{j \in N_c(i)} I_i^{j,\text{sqr}}(t)\, R_i^j(t) \tag{26}$$

where $I_i^{j,\text{sqr}}(t)$ is the square of the current. $R_i^j(t)$ is the resistance.

3.2.2 The Cost Function of the OLTC, CB, and UPFC

The limit on the number of operations of transformers and capacitor banks brings about coupling problems between time periods within the optimization cycle, increasing the complexity of the solution. This paper considers the entire cycle and integrates the objective function in the form of unit regulation cost to achieve soft constraints on the number of device operations and enhance the practicality of the reactive power optimization scheme.

The operation costs of OLTC, CB and UPFC are as follows:

$$\begin{aligned} C^{j}_{\mathrm{OLTC},i}(t) &= \Delta C_{\mathrm{OLTC}} \left| n^{j}_{\mathrm{OLTC},i}(t) - n^{j}_{\mathrm{OLTC},i}(t-1) \right| \\ C_{\mathrm{CB},i}(t) &= \Delta C_{\mathrm{CB}} \left| n_{\mathrm{CB},i}(t) - n_{\mathrm{CB},i}(t-1) \right| \\ C^{j}_{\mathrm{UPFC},i}(t) &= c Q^{j}_{\mathrm{UPFC},i}(t) \end{aligned} \tag{27}$$

where, ΔC_{OLTC} and ΔC_{CB} are the unit adjustment cost of OLTC and CB. $n^{j}_{\mathrm{OLTC},i}(t)$ and $n_{\mathrm{CB},i}(t)$ are the tap positions of OLTC and CB at time t, respectively. c is the unit reactive power cost of UPFC. $Q^{j}_{\mathrm{UPFC},i}$ is the reactive power output of UPFC between nodes i and j.

3.2.3 Constraints

(1) Constraints of the OLTC

The constraints of the OLTC restricts the position and variation of the tap of the OLTC.

$$n^{\min}_{\mathrm{OLTC}} \leqslant n^{j}_{\mathrm{OLTC},i}(t) \leqslant n^{\max}_{\mathrm{OLTC}};\ \forall i \in N_{\mathrm{b}}(z),\ j \in N^{\mathrm{t}}_{\mathrm{c}}(i),\ \forall t \tag{28}$$

$$-\Delta n^{\max}_{\mathrm{OLTC}} \leqslant \Delta n^{j}_{\mathrm{OLTC},i}(t) \leqslant \Delta n^{\max}_{\mathrm{OLTC}};\ \forall i \in N_{\mathrm{b}}(z),\ j \in N^{\mathrm{t}}_{\mathrm{c}}(i),\ \forall t \tag{29}$$

where, $n^{\min}_{\mathrm{OLTC}}$ and $n^{\max}_{\mathrm{OLTC}}$ are the minimum and maximum tap position of OLTC, respectively. $\Delta n^{j}_{\mathrm{OLTC},i}$ is the difference between the current position and the previous position. $\Delta n^{\max}_{\mathrm{OLTC}}$ is the maximum position difference for single operation of OLTC.

(2) Constraints of the CB

The constraints of the CB restricts the number of CB that are switched on.

$$0 \leqslant n_{\mathrm{CB},i}(t) \leqslant n^{\max}_{\mathrm{CB}};\ \forall i \in N_{\mathrm{b}}(z),\ \forall t \tag{30}$$

$$-\Delta n^{\max}_{\mathrm{CB}} \leqslant \Delta n_{\mathrm{CB},i}(t) \leqslant \Delta n^{\max}_{\mathrm{CB}};\ \forall i \in N_{\mathrm{b}}(z),\ \forall t \tag{31}$$

where, $n^{\max}_{\mathrm{CB}}$ is the maximum tap position of CB, $\Delta n_{\mathrm{CB},i}$ is the difference between the current position and the previous position, $\Delta n^{\max}_{\mathrm{CB}}$ is the maximum position difference for single operation of CB.

(3) Constraints of the UPFC

The constraints of the UPFC supplies controllable series injection and shunt compensation variables and their limits.

$$0 \leq V_{\mathrm{se}} \leq V^{\max}_{\mathrm{se}} = K\left|V_{10}\right| \tag{32}$$

$$-I^{\max}_{\mathrm{sh}} \leq I_{\mathrm{sh}} \leq I^{\max}_{\mathrm{sh}} \tag{33}$$

$$0 \leq \left| P_{dc} \right| \leq P^{\max}_{\mathrm{dc}} \tag{34}$$

where, V_{se} is the series injected voltage and the transmission line current. K is chosen according to the rated compensation capability of the device [43]. V_{10} is the rated voltage of node 1. $V^{\max}_{\mathrm{se}}$ is the upper limit values of

the series injected voltage and the transmission line current. I_{sh} is the shunt converter current. I_{sh}^{max} is the maximum value of the shunt converter current. P_{dc}^{max} is the maximum value of the active power exchanged of two converters.

(4) Constraints of the AC/DC hybrid power grid

The constraints of the AC/DC hybrid power grid ensure that the active power and reactive power of the power grid are within a feasible range.

$$P_{UPFC,i}^{j}(t) + \sum_{j \in N_p(i)} P_j^i(t) - \sum_{j \in N_c(i)} P_i^j(t) - P_{LOSS,i}^{j}(t) = P_i^D; \forall i \in \Omega_b, \forall t \tag{35}$$

$$Q_{UPFC,i}^{j}(t) + \sum_{j \in N_p(i)} Q_j^i(t) + Q_i^{CB}(t) - \sum_{j \in N_c(i)} Q_i^j(t) - \sum_{j \in N_c(i)} I_i^{j,sqr}(t) X_i^j(t) = Q_i^D; \forall i \in \Omega_b, \forall t \tag{36}$$

where, $N_p(i)$ is the parent node set of node i. P_i^j and Q_i^j are the active and reactive power flow values from node i to j, respectively. P_j^i and Q_j^i are the active and reactive power flow values from node j to i, respectively. X_i^j is the reactance. The reactive power injection of CB Q_i^{CB} is calculated by $Q_i^{CB} = Q_{CB,i} n_{CB,i}$, where $Q_{CB,i}$ is the reactive power capacity of each capacitor switched at node i.

(5) The constraints of the i-th LCC-HVDC are depicted in Eq. (37)

The constraints of the LCC-HVDC supply the AC/DC coupling relationships, ensuring feasibility of power flow and voltage profiles.

$$\begin{cases} P_{si,i}^{min} \le P_{si,i} \le P_{si,i}^{max} \\ Q_{si,i}^{min} \le Q_{si,i} \le Q_{si,i}^{max} \\ U_{di,i}^{min} \le U_{di,i} \le U_{di,i}^{max} \\ I_{di,i}^{min} \le I_{di,i} \le I_{di,i}^{max} \\ M_i^{min} \le M_i \le M_i^{max} \\ \delta_i^{min} \le \delta_i \le \delta_i^{max} \end{cases} \tag{37}$$

where, δ is the phase-shift angle.

3.3 The Fast-Time-Scale Optimization

3.3.1 Objective Function and Constraints

The fast-time-scale voltage control aims to minimize the total voltage deviation and the voltage fluctuation in adjacent periods. The objective function is as follows:

$$\min F_{FTC}(u) = \sum_{i=1}^{n} \left[\left| (U_{i,t} - \Delta U_{i,t}) - U_{i,t}^{ref} \right| + \left| (U_{i,t} - \Delta U_{i,t}) - U_{i,t-1} \right| \right] \tag{38}$$

where $U_{i,t}$ is the voltage amplitude at time t. $\Delta U_{i,t}$ is the variation in voltage amplitude at time t. $U_{i,t}^{ref}$ is the reference voltage.

3.3.2 The Adaptive Feedback Control Procedure

The adaptive feedback control procedure aims to adjust the control variables of OLTC, CB and UPFC based on real-time changes in the system, ensuring that the optimization objectives within the acceptable limits. The adaptive feedback control is usually carried out through the fixed-timed start [48] or fixed-value start [49]. The fixed-timed start is easy to operate, but hard to track the system's operating conditions

in a timely manner. This paper sets the initial threshold of the adaptive feedback control procedure and dynamically updates the corresponding values by evaluating the operating status of the system. This paper sets the voltage deviation as the preset threshold to calculate the voltage deviation corresponding to the slow-time-scale operation scheme. The equation of the voltage deviation is as follows:

$$U_{dev} = \frac{1}{N}\sum_{i=1}^{N}\left|U_i - U_i^{ref}\right| \tag{39}$$

where N is the number of buses.

The adaptive feedback control procedure is activated to optimize and adjust slow-time-scale operation scheme when the real-time voltage magnitude exceeds the preset threshold. Otherwise, the UPFC is further utilized for the dynamic reactive power compensation. The update equation of the threshold is as follows:

$$\rho(t) = \frac{\sum_{i=1}^{T} N_{cross}^{i}(t)}{TN} \tag{40}$$

$$\varepsilon(t+1) = \begin{cases} \min\left(\varepsilon_{\min}, \varepsilon(t) - \Delta\varepsilon\right), & \rho(t) > \rho_{high}, \\ \min\left(\varepsilon_{\max}, \varepsilon(t) + \Delta\varepsilon\right), & \rho(t) < \rho_{low}, \\ \varepsilon(t), & otherwise, \end{cases} \tag{41}$$

where $N_{cross}^{i}(t)$ is the number of nodes where the voltage deviation exceeds the threshold. T is the number of samplings in one cycle, which is 12 in this paper. ρ_{high} and ρ_{low} are the acceptable range of the crossing frequency. $\Delta\varepsilon$ is the adjustment step.

3.4 Implementation of the Proposed Method

The reactive power optimization and voltage regulation of the AC/DC hybrid power grid demonstrates strong nonlinearity and multiple constraints from both operation principles of the hybrid system and the multiple compensation devices [50]. To solve the proposed optimization problem this research employs a metaheuristic optimization algorithm, namely PSO. The PSO efficiency in handling nonlinear constraints and numerous decision variables makes it well-suited for the proposed problem. The PSO offers faster convergence, better solution diversity, and lower computational complexity. Therefore, this paper uses PSO to solve the reactive power optimization and voltage regulation of the AC/DC hybrid power grid. The discrete variables, such as the tap positions of OLTC and CB, are defined as binary variables as shown in the Eq. (42). The flowchart of the double-time-scale dynamic reactive power optimization is shown in Fig. 5. The reactive power optimization is divided into two phases in proposed method.

$$t = \sum_{j=1}^{M} a_j z_j, z_j \in \{0,1\}, \sum_{j=1}^{M} z_j = 1, j = 1, \ldots, M \tag{42}$$

where M is the number of equipments. a_j is the tap position. z_j is the binary variables.

(1) Slow-time-scale optimization: The slow-time-scale optimization focuses on minimizing the overall cost and coordinating devices with different dynamic response characteristics. In this phase, the PSO is applied to determine the optimal control variables for OLTC, CB, and UPFC, including the tap position of OLTC and CB, and the reactive power output of UPFC. If the algorithm reaches the maximum number of iterations or meets the convergence conditions, the slow-time-scale control scheme is generated, and the voltage deviation of the current operating state is calculated.

(2) Fast-time-scale optimization: Once the slow-time-scale scheme is completed, the system enters the fast-time scale phase, where the control schemes for OLTC and CB are fixed based on the results from the slow-time scale optimization. The output of UPFC is optimized in real time to minimize voltage deviations and voltage fluctuation in adjacent periods. This phase operates on a shorter time scale (5 min), ensuring that voltage stability is maintained with fine-tuned adjustments.

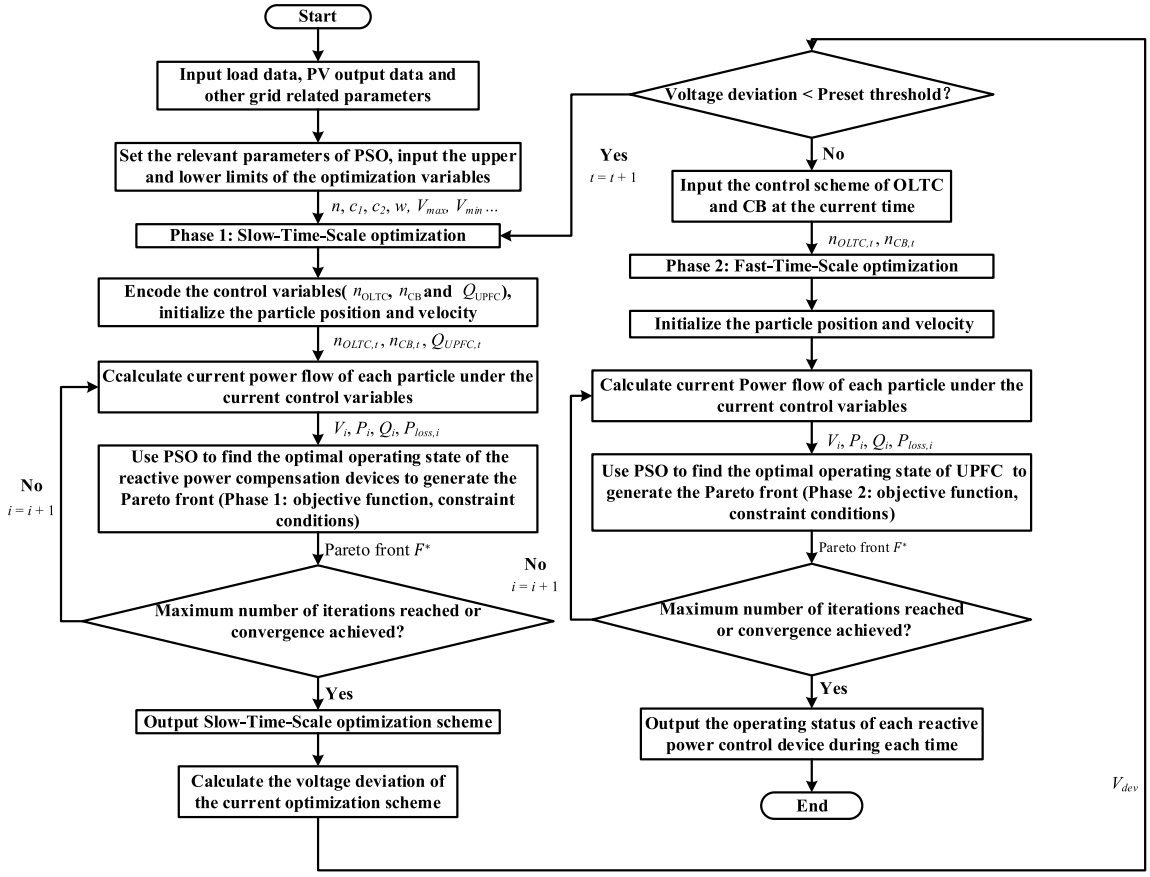

Figure 5: The flowchart of the proposed double-time-scale optimization method.

Coordination between two phases: The results from slow-time-scale provide the initial conditions for fast-time-scale optimization. When voltage deviations exceed the preset threshold, the slow-time-scale optimization is re-triggered, ensuring the system responds quickly to dynamic changes.

4 Case Study

4.1 Test System and Parameters

In order to verify the validity and feasibility of the proposed method, the simulation is carried out using Matlab 2023a on a 64-bit laptop with 2.60 GHz CPU and 16.0 GB RAM. A modified IEEE 30 bus system is used to validate the proposed method. Its network structure, load distribution, and operating characteristics can be configured to reasonably emulate a real regional power grid in Southeast China. The selection of equipment is also based on the actual power grid conditions. The topology and configuration of the system are shown in Fig. 6 and the parameters of the network can be found in [51]. The modified system has 6 generators, 20 load nodes and 41 branches. Basic operation parameters of PV, OLTCs, CBs and their

corresponding placements are shown in Table 1. The PSO population size of the fast time scale is set at 40, while that of the slow time scale is set at 50. The cognitive and social acceleration coefficients are set to c_1 = 1.5 and c_2 = 1.5, respectively. The inertia weight w = 0.7298.

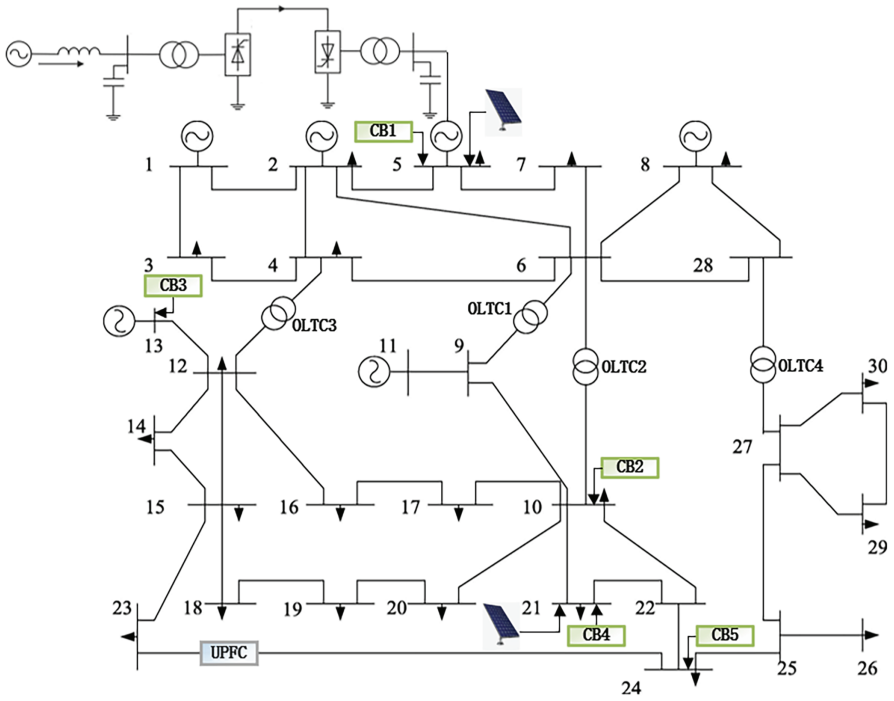

Figure 6: The modified IEEE 30 bus system.

Table 1: Parameters of the OLTCs and CBs.

Device	Location	Parameters	Constraints
OLTC1-4	Branch 6–9, 6–10, 4–12, 28–27	±8 × 1.25%	$\Delta n_{\mathrm{OLTC}}^{\max} = 5$
CB1-5	Bus 5, 10, 13, 21, 24	6 × 1 Mvar	$\Delta n_{\mathrm{CB}}^{\max} = 3$

The load and PV data is obtained by modifying a measured power load curve of the typical hourly load profile and PV plant, respectively [43]. The PV plants are located at buses 5 and 21 with an individual installed capacity of 30 MW and the inverter power factor ranges between 0.9 to 1.0.

The LCC-HVDC system in this study is configured in a monopolar scheme, with its terminal connected to Bus 5. The LCC-HVDC control mode is the constant power of the rectifier side varies from 70% to 100% of the rated power at 6.0 p.u., and the constant voltage of the inverter side is set at 1.0 p.u. The commutation reactance is 0.006 p.u., and the resistance of the LCC-HVDC tie line is 0.01 p.u. The LCC-HVDC power curve of the rectifier side is shown in Fig. 7. The LCC-HVDC transmits full rated power during the peak load periods and 70% rated power during the valley load periods.

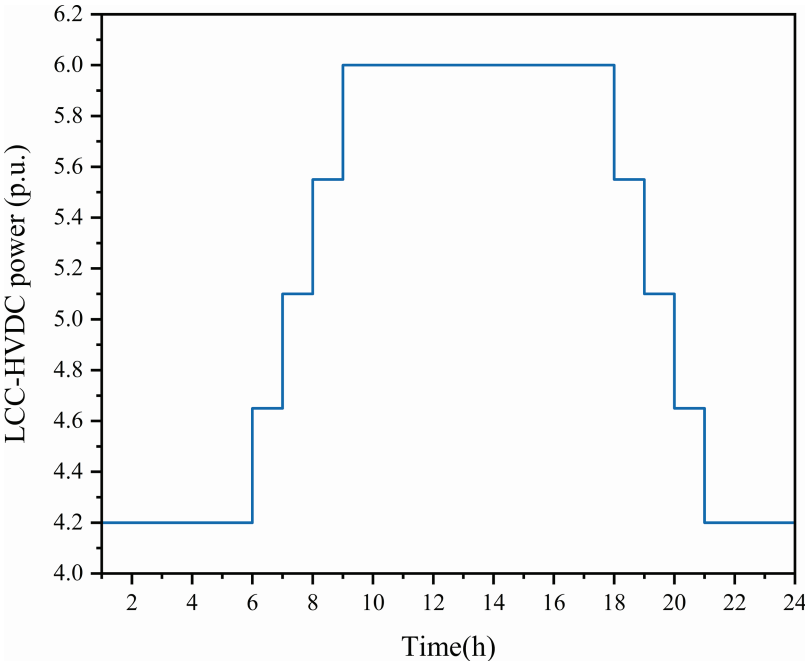

Figure 7: LCC-HVDC power transmission profile of the rectifier side.

The UPFC is located at branch 23–24 and close to node 23. The parameters and constraints of UPFC is shown in Table 2. The control intervals of the slow-time scale and fast-time scale are designed as 1 h and 5 min. The number of the prediction steps is designed as 3 and 5, respectively. The tolerance factor ε is 1×10^{-3} and the adjustable parameter ρ is 2×10^{-4}. The details of the power loss cost as well as the unit adjustment costs of OLTC, CB and UPFC are in [19].

Table 2: The parameters of the UPFC.

X_{sh}/pu	X_{se}/pu	$U_{sh,max}$/pu	$U_{se,max}$/pu	$S_{sh,max}$/pu
0.05	0.05	1.10	0.40	1.10

The proposed method is implemented in MATLAB R2024a on an i5–14600 core PC with 32 GB RAM. Three scenarios are studied to verify the effectiveness of the proposed method.

4.2 Simulation Result

The average computation times were approximately 45 s for the fast-time-scale optimization and 4 min for the slow-time-scale optimization. The voltage regulation cost weight coefficients calculated based on the trajectory sensitivity of the slow-time scale are W_{UPFC} = 0.3998, W_{OLTC} = 0.3227, and W_{CB} = 0.2775. The OLTC and CB with smaller coefficients of the trajectory-sensitivity weight are prioritized in the optimization, which matches the operation principle of discrete devices in practical. The coefficient of UPFC device is the largest based on the trajectory-sensitivity weighting mechanism to preserve sufficient dynamic reserve of reactive power for the fast-time-scale adjustment. In other words, the trajectory-sensitivity-based weighting mechanism guides the slow-time-scale. Figs. 8–10 present the tap positions of OLTC and CB, and the reactive power output of UPFC in the slow-time-scale, respectively.

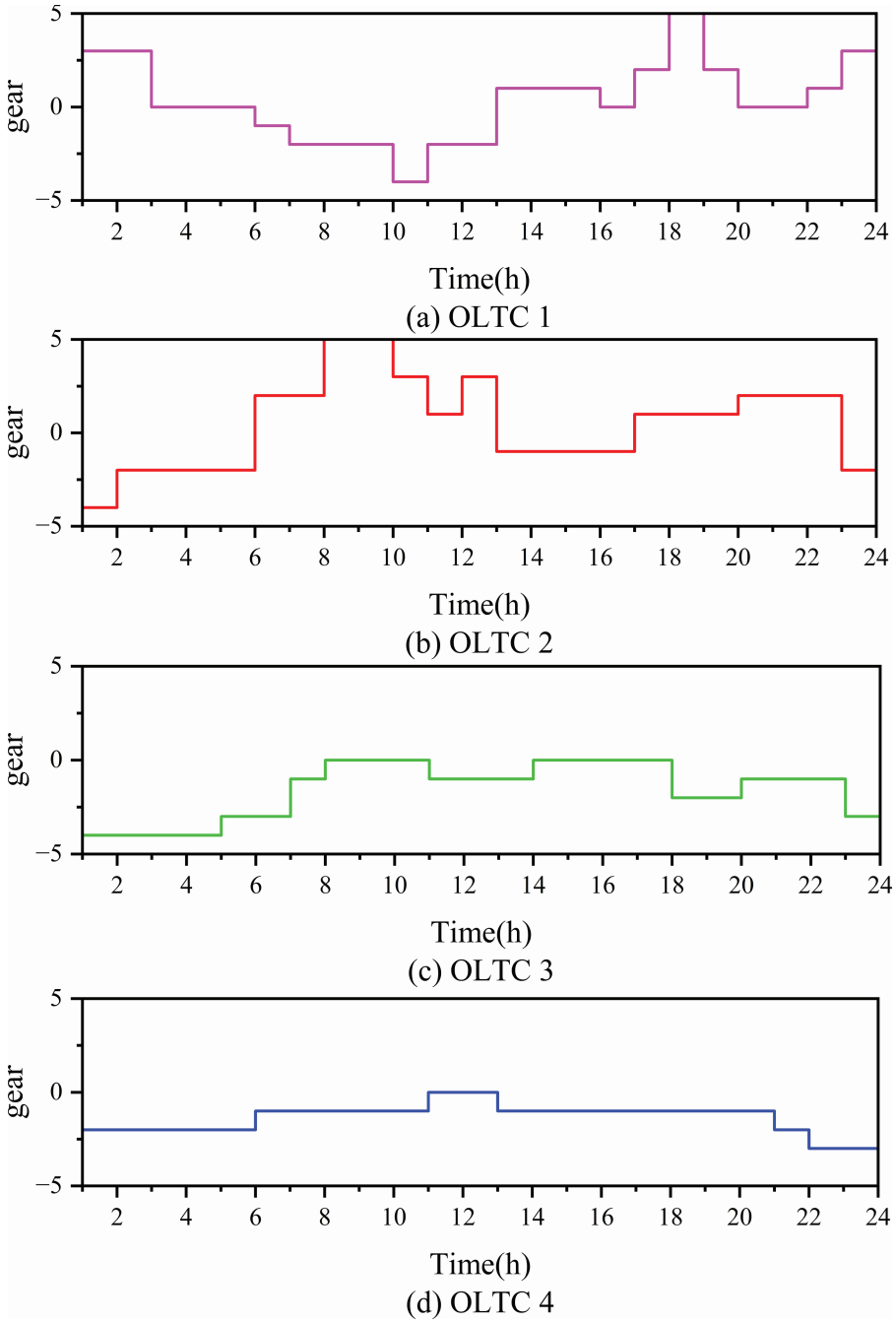

Figure 8: OLTC gear changing logic.

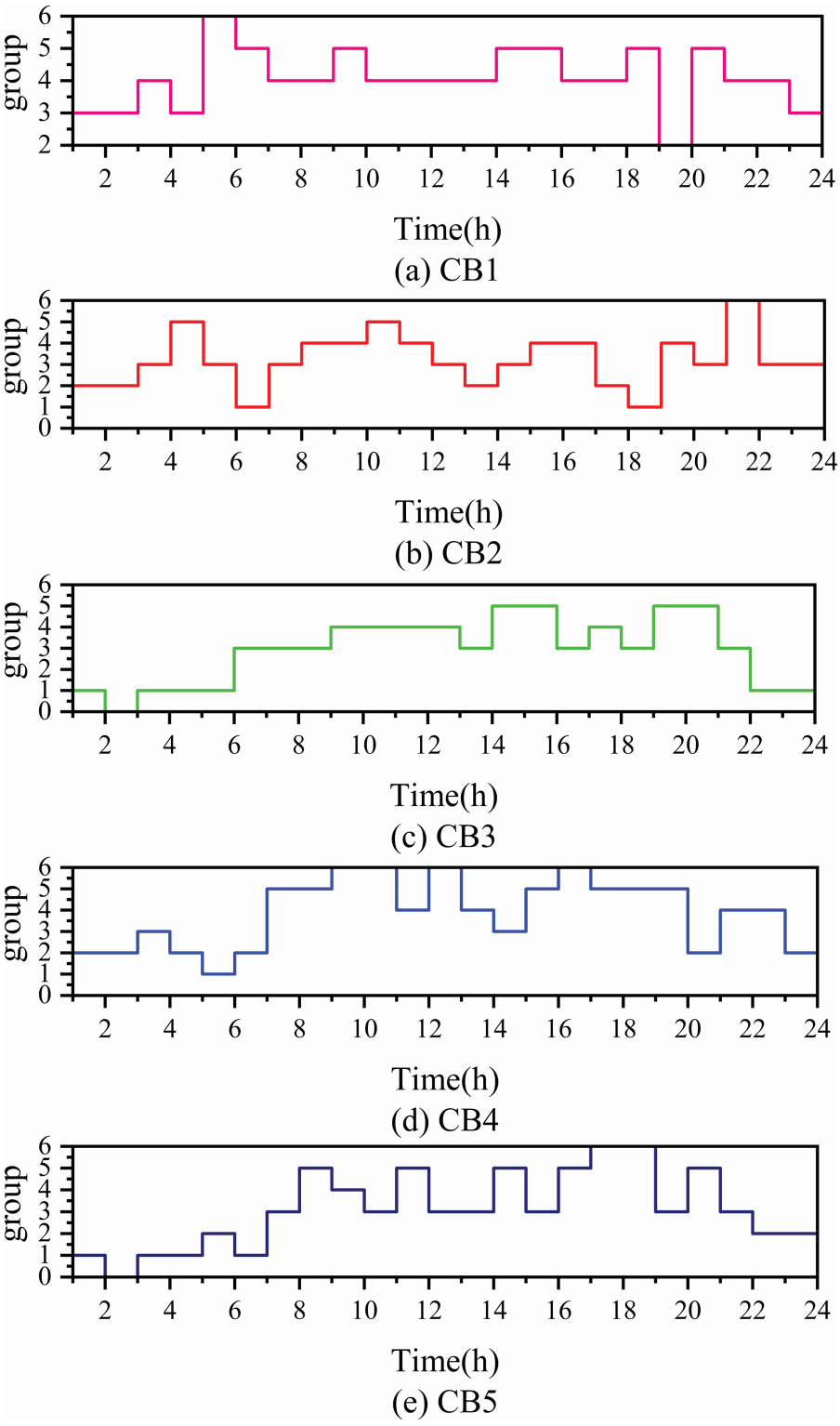

Figure 9: CB switching logic.

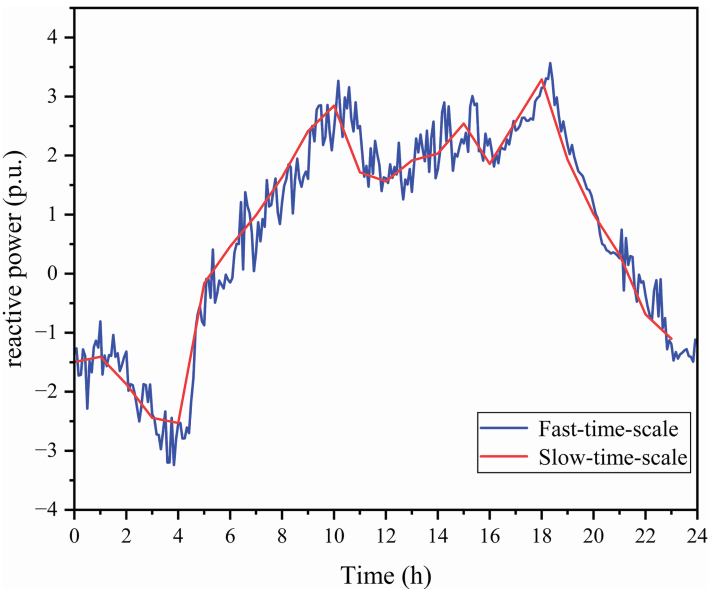

Figure 10: UPFC reactive power output.

Fig. 8 shows the tap positions of the OLTCs of the proposed method. As shown in the figure, the tap positions are generally higher during the peak load period (10:00~15:00) and lower during the off-peak period (23:00~05:00), which conforms to the principle of reverse voltage regulation. The four OLTC devices have a total of 88 tap position changes. OLTC2, located near PV units and loads, operated most frequently to minimize the active power losses. In contrast, OLTC4, located far from the load center, exhibited the least activeness with only 8 times of the tap change throughout the day.

Fig. 9 illustrates the switching operations of 5 CBs with total 128 actions. CB3, located at the bus with strong support from the generator, required the least number of operations (18 changes). CB1, also near a generator but influenced by adjacent PV plant and loads, undergoes a more frequent operations (20 changes) than CB3. CB2 changes most frequently and is located close to the load center.

Fig. 10 shows the reactive power output of the UPFC of slow-time-scale and fast-time-scale. It can be seen that the UPFC is affected by the demand of dynamic reactive power reserve of the fast-time scale, and its output range is between [−3, 4] Mvar. The reactive power output of the UPFC is consistent with the trend of demand of reactive power which is rising in the daytime rise and falling at night. The reactive power output of the UPFC rises from 0.9912 to 2.8455 Mvar from 08:00 to 11:00 to compensate the morning peak demand. At night (23:00 to 05:00), the UPFC absorbs reactive power reversely, which demonstrates its ability for bi-directional capability of reactive power regulation. Slow-time-scale regulates the UPFC output hourly and fast-time-scale updates the reactive power output of UPFC at 5-min interval. Obviously, the fast-time-scale has better ability to keep up with the fluctuations of the PV and load.

4.3 Scenario 1: No Control

In this scenario, the system operates with no additional compensation. As shown in Fig. 11, the voltage profiles of 1 a.m., 7 a.m., 13 p.m. and 19 p.m. all exhibit severe over-limit conditions. At 1:00, the valley low load profile results in a severe under-voltage issue and the minimum voltage magnitude is 0.874 p.u. At 7:00, 13:00, and 19:00, the system experiences pronounced over-voltage conditions and the maximum voltage magnitude is 1.085 p.u.

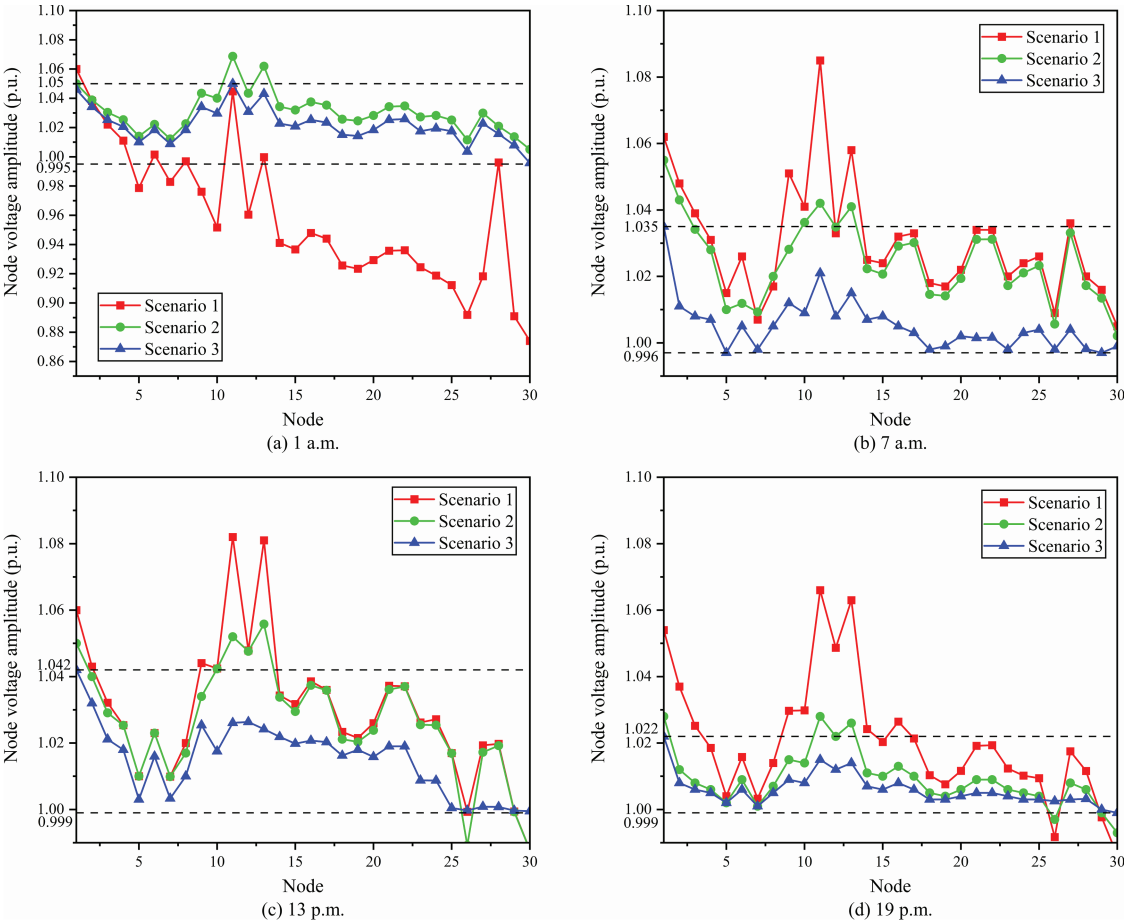

Figure 11: System voltage at 1 a.m., 7 a.m., 13 p.m. and 19 p.m.

4.4 Scenario 2: Only the Slow-Time-Scale Optimization

In this scenario, a slow-time-scale control method is implemented to address the voltage issue. The results, presented in Fig. 11, demonstrate that the voltage profiles in Scenario 2 which are markedly improved at both 1 a.m. and 19 p.m. compared to the baseline Scenario 1. However, the control method proves inadequate during the high PV generation hours of 7 a.m. and 13 p.m. The substantial power injection from the PV systems during these hours leads to the reversed power flow and elevated voltage magnitudes with the maximum value 1.042 and 1.056 p.u. The slow-time-scale control method improves the node voltage profile to a certain extent, but its impact is limited. The reason is the 1 h control interval is too large compared to the PV and load fluctuations. Consequently, a considerable number of nodes suffer from under- and over-voltage issues, showing the limitation of this method in dealing with voltage violations.

4.5 Scenario 3: The Double-Time-Scale Optimization

In this scenario, the double-time-scale voltage control method is implemented to address the voltage issues.

Fig. 11 presents the voltage curves under cases representing four different PV and load outputs including 1 a.m. with low PV and low load, 7 a.m. with medium PV and high load, 13 p.m. with high PV and low load, and 19 p.m. with low PV and high load. As shown in Fig. 11, the proposed method achieves a great improvement of the voltage profile of all four moments compared to both Scenario 1 and 2. The voltage

magnitudes of all nodes are effectively maintained within the safe operation range. Quantitative analyses demonstrate the improvements of Scenario 3 compared to both Scenario 1 and 2. The average system voltage deviations of Scenario 3 at 1 a.m., 7 a.m., 13 p.m. and 19 p.m. are reduced by 3.63%, 3.31%, 3.17%, and 1.75% compared to Scenario 1, respectively. Similarly, the average system voltage deviations of Scenario 3 at 1 a.m., 7 a.m., 13 p.m. and 19 p.m. are reduced by 1.41%, 1.44%, 2.02%, and 0.62% compared to Scenario 2, respectively. The maximum and minimum voltages of each scheme are shown in the Table 3. It can be seen from Fig. 11, the regulation effect of Scenario 3 at the time with high PV output (7 a.m. and 13 p.m.) is significantly improved compared to Scenario 2. The reason is that high PV output also brings about frequent fluctuations in PV output, led to rapid voltage swings. The slow-time-scale voltage control method is insufficient to control rapid voltage swings. By implementing the additional fast-time scale control method, the frequent variations of both the PV and load can be managed better by the 5 min optimization of the reactive power. The method proposed in this paper can suppress voltage fluctuations and improve the overall voltage profile of the system.

Table 3: The maximum and minimum voltages of each time in Scenario 3 (p.u.).

	1 a.m.	7 a.m.	13 p.m.	19 p.m.
Maximum voltage	1.050	1.035	1.042	1.022
Minimum voltage	0.995	0.996	0.999	0.999

Table 4 shows the voltage magnitude of node 5 which is the HVDC terminal. The voltage profiles of the HVDC terminal are all within a safe operation range and the method proposed in this paper has the superior controllability compared to the other two scenarios.

Table 4: The volage magnitudes of the HVDC terminal (p.u.).

	1 a.m.	7 a.m.	13 p.m.	19 p.m.
Scenario 1	0.979	1.015	1.010	1.004
Scenario 2	1.014	1.010	1.010	1.002
Scenario 3	1.010	0.997	1.003	1.002

Table 5 shows the losses for three scenarios. The unit adjustment costs of OLTC, CB and UPFC are in Table A1. The total loss is 426.64 MW in Scenario 1, which is reduced to 369.02 MW in Scenario 2 and 374.84 MW in Scenario 3. The total losses of Scenario 2 and 3, compared to no control, are reduced by 13.51% and 12.14% compared to Scenario 1, respectively. Higher cost in Scenario 3 due to increased UPFC usage for voltage stability. Based on the analysis of the objective function and voltage profiles in Fig. 9, it can be seen that Scenario 3 sacrifices a certain degree of network loss to realize the purpose of voltage regulation. Hence, the total cost of Scenario 3 is slightly higher than that of Scenario 2.

Table 5: Network loss and total cost.

	Scenario 1	Scenario 2	Scenario 3
Total Network loss/MW	426.6437	369.0200	374.8438
Total cost/Yuan	/	170,350.986	172,639.326

In conclusion, the case study confirms that the proposed double-time-scale voltage control method improves the overall voltage profiles and system stability. The proposed method also achieves a balance between the economic and operation aspects, making it a viable solution for the future AC/DC hybrid grids with high renewable energy integration.

5 Conclusion

This paper proposes a double-time-scale dynamic reactive power optimization method for AC/DC hybrid power grid with UPFC to address the problem considering the fluctuations and uncertainty of renewable energy. The trajectory sensitivity is used to construct the voltage regulation cost weight coefficients which is the key element of the distribution mechanism incorporating various regulation devices. The slow-time-scale (1 h) optimization aims to optimize the control variables of OLTC, CB and UPFC with the goal of minimizing the total cost, and preserves sufficient dynamic reactive power regulation capability. The fast-time-scale (5 min) optimization aims to optimize the output of UPFC in real time with the goal of minimizing voltage fluctuation by implementing the adaptive feedback control mechanism to adjust the real-time reactive power output of the UPFC. The simulation based on the modified IEEE 30 bus system shows that the network loss is reduced by 12.14% with the proposed double-time-scale optimization method. The deviation and fluctuation of the system voltage are also significantly reduced especially at the LCC-HVDC terminal. By fully utilizing the bi-directional compensation ability of the UPFC and coordinating all the regulation devices, the voltage stability and total cost of the system are both improved.

The current study has several limitations. (1) The robustness and convergence behavior of PSO in mixed-integer optimization is not systematically analyzed. (2) The scalability of the proposed framework is only validated on the modified IEEE 30-bus system, and its computational performance on larger grids has not been evaluated. (3) The uncertainty introduced by renewable-generation forecasts is not fully quantified in the present formulation. (4) Coordination issues among multiple UPFCs are not considered.

Future work will (1) investigate PSO robustness and convergence for mixed-integer settings via sensitivity and multi-run analyses, (2) conduct scalability tests on larger grids, (3) extend the framework to coordinated optimization of UPFC with wind generation and energy storage under renewable uncertainty, (4) extend the proposed approach by modeling communication delays and sampling intervals and evaluating their impacts on control performance and solution reliability, (5) develop coordinated control strategies for multiple UPFCs, including decentralized or hierarchical coordination schemes.

Acknowledgement: Not applicable.

Funding Statement: Project Supported by Science and Technology Project of State Grid Jiangsu Electric Power Company: Research on Weak Node Identification and UPFC Response Strategy for AC/DC Hybrid Receiving Urban Power Grid (J2024013).

Author Contributions: The authors confirm contribution to the paper as follows: study conception or design: Wei Yin. Author; data collection: Jun Wang. Author; data analysis or interpretation: Ming Tong. Author; conceptualization: Zhijun Chen. Author; methodology: Ke Zhang. Author; writing the paper: Meiqing Huang. Author; writing the paper: Ran Gu. Author; validation: Keman Lin. Author. All authors reviewed and approved the final version of the manuscript.

Availability of Data and Materials: Due to the nature of this research, participants of this study did not agree for their data to be shared publicly, so supporting data is not available.

Ethics Approval: Not applicable.

Conflicts of Interest: The authors declare no conflicts of interest.

Nomenclature

Abbreviations

AC/DC	Alternating current/Direct current
CB	Capacitor bank
FACTS	Flexible AC transmission system
UPFC	Unified power flow controller
LCC-HVDC	Line-commutated converter high voltage direct current
OLTC	On-load tap changer
PSO	Particle swarm optimization
PV	Photovoltaic
SVC	Static var compensator

Parameters

α, β	The adjustable parameters of the Beta model
η	The photoelectric conversion efficiency
x	The input parameter of the Gamma function
r	The solar irradiance value
A	The total area of photovoltaic panels
$P_{\mathrm{PV,max}}$	The maximum output by PV
X_i^j	The equivalent reactance between node i to node j
R_i^j	The equivalent resistance between node i to node j
a_i	The impedance angle
Y_i^j	The equivalent admittance between node i to node j
Z_R	The impedance of the UPFC at the receiving terminal
ω	The angular frequency of the UPFC
M	The modulation index of the converter of the UPFC
$Q_{\mathrm{max+}}$, $Q_{\mathrm{max-}}$	The adjustable reactive power range of UPFC
N	The voltage ratio of the OLTC
ΔV_{OLTC}	The voltage ratio corresponding to a single gear of OLTC
n_{OLTC}	The tap position of OLTC
Ω_b	The node set
N_c	The child node set
N_p	The parent node set
W_{OLTC}, W_{CB}, W_{UPFC}	The voltage regulation cost weight coefficients of OLTC, CB and UPFC
π_t	The unit cost of network loss
u_{base}	The basic value of the control variable
V_{base}	The basic value of the voltage
ΔC_{OLTC}, ΔC_{CB}	The unit adjustment cost of OLTC and CB
c	The unit reactive power cost of UPFC
n_{OLTC}^{min}, n_{OLTC}^{max}	The minimum and maximum tap position of OLTC
$n_{\mathrm{CB}}^{\max}$	The maximum tap position of CB
K	The parameter of the compensation capability
$I_{\mathrm{sh}}^{\max}$	The maximum value of the shunt converter current.
$P_{\mathrm{dc}}^{\max}$	The maximum value of the active power exchanged of two converters
$U_{i,t}^{ref}$	The reference voltage
T	The number of samplings in one cycle
ρ_{high}, ρ_{low}	The acceptable range of the crossing frequency
$\Delta\varepsilon$	The adjustment step
M	The number of equipments

Variables

F	The probability value
$P_{\mathrm{PV},t}$	The actual output by PV at time t
Γ	The gamma function value
P_{si}, Q_{si}	The active and reactive power absorbed by the converter station from the AC system
U_{si}	The voltage magnitude of the AC system
θ_{si}	The voltage phase angle of the AC system
P_{ci}, Q_{ci}	The active and reactive power entering the converter bridge arm
U_{ci}	The voltage magnitude of the converter station
θ_{ci}	The voltage phase angle of the converter station
δ_i	The phase angle difference between the AC and DC buses
P_{di}	The active power transmitted by the DC system
U_{di}	The voltage of the DC system
I_{di}	The current of the DC system
V_1	The bus voltage of the UPFC input terminal
V_{12}	The injection voltage of the UPFC to the power grid
V_{R}	The voltage of the UPFC at the receiving terminal
I	The line current
I_{sh}	The current between the AC network and the shunt converter
V_{sh}	The voltage of the shunt converter
L_{sh}	The inductance of the shunt converter
V_{dc}	The voltage of DC link capacitor of the UPFC
P_{12}, Q_{12}	The active and reactive power injected into the power grid by the UPFC
U_i	The voltage at node i
$C^j_{OLTC,i}$, $\mathrm{C}_{\mathrm{CB,i}}$, $C^j_{UPFC,i}$	The reactive power regulation cost of OLTC, CB and UPFC
P^j_i, Q^j_i	The active and reactive power flow values from node i to node j
$P_{\mathrm{LOSS},ji}(t)$	The network loss between node i and j at time t
$\Phi_x \Phi_y$	The change trajectories of state variables and algebraic variables
$x(t)$, $y(t)$	The state variables and algebraic variables at time t
$n^j_{OLTC,i}$, $n_{CB,i}$	The tap positions of OLTC and CB at time t
Q^{CB}_i	The reactive power capacity of each capacitor switched at node i
$Q^j_{UPFC,i}$	The reactive power output of UPFC between nodes i and j
V_{se}	The series injected voltage and the transmission line current
V_{10}	The rated voltage of node 1
$V^{\max}_{\mathrm{se}}$	The upper limit values of the series injected voltage and the transmission line current
I_{sh}	The shunt converter current
N^i_{cross}	The number of nodes where the voltage deviation exceeds the threshold

Appendix A

Table A1: The unit adjustment costs of OLTC, CB and UPFC.

Equipment	OLTC	CB	UPFC
Costs	60 yuan/group	50 yuan/group	150 yuan/Mvar

References

1. Valencia F, Palma-Behnke R, Ortiz-Villalba D, De La Quintana A, Rahmann C, Cifuentes R. Special protection systems: challenges in the Chilean market in the face of the massive integration of solar energy. IEEE Trans Power Deliv. 2017;32(1):575–84. doi:10.1109/TPWRD.2016.2558518.
2. Jafari MR, Parniani M, Ravanji MH. Decentralized control of OLTC and PV inverters for voltage regulation in radial distribution networks with high PV penetration. IEEE Trans Power Deliv. 2022;37(6):4827–37. doi:10.1109/TPWRD.2022.3160375.
3. Hasheminamin M, Agelidis VG, Salehi V, Teodorescu R, Hredzak B. Index-based assessment of voltage rise and reverse power flow phenomena in a distribution feeder under high PV penetration. IEEE J Photovolt. 2015;5(4):1158–68. doi:10.1109/JPHOTOV.2015.2417753.
4. Zhang Y, Meng X, Shotorbani AM, Wang L. Minimization of AC-DC grid transmission loss and DC voltage deviation using adaptive droop control and improved AC-DC power flow algorithm. IEEE Trans Power Syst. 2021;36(1):744–56. doi:10.1109/TPWRS.2020.3020039.
5. Zhang J, Ji Y, Zhou J, Jia Y, Shi G, Wang H. Cooperative AC/DC voltage margin control for mitigating voltage violation of rural distribution networks with interconnected DC link. IEEE Trans Power Deliv. 2025;40(2):1014–29. doi:10.1109/TPWRD.2025.3535712.
6. Feng N, Feng Y, Su Y, Zhang Y, Niu T. Dynamic reactive power optimization strategy for AC/DC hybrid power grid considering different wind power penetration levels. IEEE Access. 2024;12:187471–82. doi:10.1109/ACCESS.2024.3392851.
7. Nejabatkhah F, Li YW. Overview of power management strategies of hybrid AC/DC microgrid. IEEE Trans Power Electron. 2015;30(12):7072–89. doi:10.1109/TPEL.2014.2384999.
8. He L, Li Y, Shuai Z, Guerrero JM, Cao Y, Wen M, et al. A flexible power control strategy for hybrid AC/DC zones of shipboard power system with distributed energy storages. IEEE Trans Ind Inf. 2018;14(12):5496–508. doi:10.1109/tii.2018.2849201.
9. Alencar MV, da Silva DN, Nepomuceno L, Martins ACP, Balbo AR, Soler EM. Discrete optimal power flow with prohibited zones, multiple-fuel options, and practical operational rules for control devices. Appl Energy. 2024;358(1):122545. doi:10.1016/j.apenergy.2023.122545.
10. Choeum D, Choi DH. OLTC-induced false data injection attack on volt/VAR optimization in distribution systems. IEEE Access. 2019;7:34508–20. doi:10.1109/ACCESS.2019.2904959.
11. Wu X, Wang R, Wang Y, Wang L. A novel UPFC model and its convexification for security-constrained economic dispatch. IEEE Trans Power Syst. 2022;37(6):4202–13. doi:10.1109/TPWRS.2022.3148090.
12. Ghaedi S, Abazari S, Arab Markadeh G. Transient stability improvement of power system with UPFC control by using transient energy function and sliding mode observer based on locally measurable information. Measurement. 2021;183(1):109842. doi:10.1016/j.measurement.2021.109842.
13. Mahmood H, Michaelson D, Jiang J. Accurate reactive power sharing in an islanded microgrid using adaptive virtual impedances. IEEE Trans Power Electron. 2015;30(3):1605–17. doi:10.1109/TPEL.2014.2314721.
14. Mahmood H, Michaelson D, Jiang J. Reactive power sharing in islanded microgrids using adaptive voltage droop control. IEEE Trans Smart Grid. 2015;6(6):3052–60. doi:10.1109/TSG.2015.2399232.
15. Hoang TV, Lee HH. Distributed control scheme for accurate reactive power sharing with enhanced voltage quality for islanded microgrids. J Power Electron. 2020;20(2):601–13. doi:10.1007/s43236-020-00047-1.
16. Fan Y, Yang Y, Wu F, Qiu H, Ye P, Xu W, et al. Coordinated reactive power-voltage control in distribution networks with high-penetration photovoltaic systems using adaptive feature mode decomposition. Energies. 2025;18(11):2866. doi:10.3390/en18112866.
17. Zhang Z, da Silva FF, Guo Y, Bak CL, Chen Z. Double-layer stochastic model predictive voltage control in active distribution networks with high penetration of renewables. Appl Energy. 2021;302(C):117530. doi:10.1016/j.apenergy.2021.117530.
18. Chi Y, Tao A, Xu X, Wang Q, Zhou N. An adaptive many-objective robust optimization model of dynamic reactive power sources for voltage stability enhancement. J Mod Power Syst Clean Energy. 2023;11(6):1756–69. doi:10.35833/MPCE.2022.000431.

19. Meng L, Yang X, Zhu J, Wang X, Meng X. Network partition and distributed voltage coordination control strategy of active distribution network system considering photovoltaic uncertainty. Appl Energy. 2024;362:122846. doi:10.1016/j.apenergy.2024.122846.
20. Oskouei MZ, Mohammadi-Ivatloo B, Erdinç O, Erdinç FG. Optimal allocation of renewable sources and energy storage systems in partitioned power networks to create supply-sufficient areas. IEEE Trans Sustain Energy. 2021;12(2):999–1008. doi:10.1109/TSTE.2020.3029104.
21. Zhou H, Liang J, Du X, Wu M. Multi-timescale reactive power optimization and regulation method for distribution networks under a multi-source interaction environment. Processes. 2024;12(10):2254. doi:10.3390/pr12102254.
22. Zhao B, Guo CX, Cao YJ. A multiagent-based particle swarm optimization approach for optimal reactive power dispatch. IEEE Trans Power Syst. 2005;20(2):1070–8. doi:10.1109/TPWRS.2005.846064.
23. Zheng W, Wu W, Zhang B, Sun H, Liu Y. A fully distributed reactive power optimization and control method for active distribution networks. IEEE Trans Smart Grid. 2016;7(2):1021–33. doi:10.1109/TSG.2015.2396493.
24. Hu A, Li G, Zhang T, Zhou M, Wang J. Probabilistic feasible region characterization of active distribution networks driven by data-model fusion. IEEE Trans Ind Appl. 2025;61(2):2791–802. doi:10.1109/TIA.2025.3529796.
25. Liao H, Abdelrahman S, Guo Y, Milanović JV. Identification of weak areas of network based on exposure to voltage sags: part II: assessment of network performance using sag severity index. IEEE Trans Power Deliv. 2015;30(6):2401–9. doi:10.1109/TPWRD.2014.2362957.
26. Xue C, Cao G, Wang ZM, Ma XP. Research on the reactive power and voltage control method for AC-DC hybrid systems based on the whale swarm algorithm. Power Syst Clean Energy. 2023;39(9):67–73. (In Chinese).
27. Zand M, Nasab MA, Padmanaban S, Maroti PK, Muyeen SM. Sensitivity analysis index to determine the optimal location of multi-objective UPFC for improvement of power quality parameters. Energy Rep. 2023;10(4):431–8. doi:10.1016/j.egyr.2023.06.028.
28. Wu W, Tian Z, Zhang B. An exact linearization method for OLTC of transformer in branch flow model. IEEE Trans Power Syst. 2017;32(3):2475–6. doi:10.1109/TPWRS.2016.2603438.
29. Haque MM, Ali MS, Wolfs P, Blaabjerg F. A UPFC for voltage regulation in LV distribution feeders with a DC-link ripple voltage suppression technique. IEEE Trans Ind Appl. 2020;56(6):6857–70. doi:10.1109/TIA.2020.3023068.
30. Sharma S, Sabitha B, Prabhakaran A, Chavan M, Srivastava R. A hybrid swarm intelligence approach for resolving reactive power dispatch issues in power system: optimal placement and sizing of UPFC. Adv Eng Softw. 2022;170(3):103149. doi:10.1016/j.advengsoft.2022.103149.
31. Sun R, Zhu ZR, Wei ZN, Sun GQ, Liao XX. Multi-objective and multi-stage reactive power optimization algorithm for power system considering UPFC. Electr Power Eng Technol. 2020;39(1):76–85. (In Chinese).
32. Paul S, Sharma A, Padhy NP. Risk constrained energy efficient optimal operation of a converter governed AC/DC hybrid distribution network with distributed energy resources and volt-VAR controlling devices. IEEE Trans Ind Appl. 2021;57(4):4263–77. doi:10.1109/TIA.2021.3081526.
33. Wang X, Gu L, Liang D. Decentralized and multi-objective coordinated optimization of hybrid AC/DC flexible distribution networks. Front Energy Res. 2021;9:762423. doi:10.3389/fenrg.2021.762423.
34. Sun S, Yuan Z, Chen D, Li Z, Tang X, Song Y, et al. Research on coordinated control of dynamic reactive power sources of DC blocking and commutation failure transient overvoltage in new energy transmission. Energies. 2025;18(9):2349. doi:10.3390/en18092349.
35. Xiao D, Sun H, Nikovski D, Kitamura S, Mori K, Hashimoto H. CVaR-constrained stochastic bidding strategy for a virtual power plant with mobile energy storages. In: Proceedings of the 2020 IEEE PES Innovative Smart Grid Technologies Europe (ISGT-Europe); 2020 Oct 26–28; The Hague, Netherlands. p. 1171–5. doi:10.1109/ISGT-Europe47291.2020.9248799.
36. Xiao D, Deng W, Liu B, Huang W, Zhu Z. Game-theoretic energy scheduling for community multi-energy system with electric vehicle aggregator leveraging quantum swarm intelligence. Int J Electr Power Energy Syst. 2025;172:111200. doi:10.1016/j.ijepes.2025.111200.
37. Guo Y, Wu Q, Gao H, Huang S, Zhou B, Li C. Double-time-scale coordinated voltage control in active distribution networks based on MPC. IEEE Trans Sustain Energy. 2020;11(1):294–303. doi:10.1109/tste.2018.2890621.

38. Zhang Z, da Silva FF, Guo Y, Bak CL, Chen Z. Coordinated voltage control in unbalanced distribution networks with two-stage distributionally robust chance-constrained receding horizon control. Renew Energy. 2022;198(C):907–15. doi:10.1016/j.renene.2022.08.086.
39. Gaur B, Ucheniya R, Saraswat A. Real power transmission loss minimization and bus voltage improvement using UPFC. In: Advances in communication, devices and networking. Singapore: Springer; 2020. p. 1–9. doi:10.1007/978-981-15-4932-8_1.
40. Yeung C, Wang J, Du Y, Cao J, Zhou Q, Ding Y, et al. Comprehensive analysis of solar irradiance and photovoltaic power generation: case studies in Wuhan and Zhangbei. China IEEE Trans Ind Applicat. 2025;61(6):8307–17. doi:10.1109/tia.2025.3569247.
41. Fernandez-Jimenez LA, Monteiro C, Ramirez-Rosado IJ. Short-term probabilistic forecasting models using Beta distributions for photovoltaic plants. Energy Rep. 2023;9:495–502. doi:10.1016/j.egyr.2023.01.059.
42. Liu D, Zou C, Li X, Lin B, Liu J, Jin T. Suppression of continuous commutation failure in LCC-HVDC transmission based on improved virtual synchronous generator control for energy storage system. Int J Electr Power Energy Syst. 2024;159:110018. doi:10.1016/j.ijepes.2024.110018.
43. Ndjankeu NM, Moulum PA, Kenfack P, Naoussi SRD. Modern sensitivity index-based optimal UPFC location for power quality enhancement in the Southern Cameroon interconnected grid considering the feasibility of the load flow under N-k contingency scenarios. Energy Rep. 2025;13:5160–86. doi:10.1016/j.egyr.2025.04.049.
44. Li Z, Wu Q, Chen J, Huang S, Shen F. Double-time-scale distributed voltage control for unbalanced distribution networks based on MPC and ADMM. Int J Electr Power Energy Syst. 2023;145:108665. doi:10.1016/j.ijepes.2022.108665.
45. Zhao Q, Pang L, Li X, Wang S, Yin Z, Guo L. Dual-timescale active and reactive power collaborative optimization for voltage regulation based on multiobjective deep reinforcement learning in distribution network. Sustain Energy Grids Netw. 2025;43:101806. doi:10.1016/j.segan.2025.101806.
46. Buragohain U, Mir AS, Senroy N. Transient stability assessment of a DFIG-WTG system using trajectory sensitivity analysis. IEEE Trans Power Syst. 2024;39(4):5818–28. doi:10.1109/TPWRS.2023.3345347.
47. Song ZQ, Huang YH, Zhao HS, Xu JZ, Zhao CY, Jia XF. Applicability analysis of power flow calculation methods for AC/DC hybrid connected power grid with multi-type DC. Electr Power Autom Equip. 2024;44:190–6. (In Chinese). doi:10.16081/j.epae.202307004.
48. Lin X, Wu C, Yao W, Liu Z, Shen X, Xu R, et al. Observer-based fixed-time control for permanent-magnet synchronous motors with parameter uncertainties. IEEE Trans Power Electron. 2023;38(4):4335–44. doi:10.1109/tpel.2022.3226033.
49. Menon GS, Vinopraba T, Lithika J, Kannan S. Soft constrained warm start based MPC-PD approach for real time control of underactuated systems. IEEE Lat Am Trans. 2025;23(9):762–9. doi:10.1109/TLA.2025.11119486.
50. Chauhan D, Yadav A, Cho SB. AEFA-FDB: a score-based artificial electric field algorithm for optimal reactive power dispatch problem with renewable and load demand uncertainties. Appl Soft Comput. 2025;180:113292. doi:10.1016/j.asoc.2025.113292.
51. Ji BX, Liu HH, Cheng P, Ren XY, Pi HD, Li LL. Phased optimization of active distribution networks incorporating distributed photovoltaic storage system: a multi-objective coati optimization algorithm. J Energy Storage. 2024;91:112093. doi:10.1016/j.est.2024.112093.